IOP Publishing Journal of Physics B: Atomic, Molecular and Optical Physics
J. Phys. B: At. Mol. Opt. Phys. **53** (2020) 095202 (12pp) https://doi.org/10.1088/1361-6455/ab7641

Dynamics of $H(^2S) + CH(X^2\Pi)$ reactions based on a new $CH_2(\tilde{X}^3A'')$ surface via extrapolation to the complete basis set limit

Lulu Zhang[1], Dong Liu[1], Daguang Yue[1], Yuzhi Song[2] and Qingtian Meng[2]

[1] School of Science, Shandong Jiaotong University, 250357 Jinan, People's Republic of China
[2] Shandong Province Key Laboratory of Medical Physics and Image Processing Technology, School of Physics and Electronics, Shandong Normal University, 250358 Jinan, People's Republic of China

E-mail: qtmeng@sdnu.edu.cn

Received 8 October 2019, revised 17 January 2020
Accepted for publication 13 February 2020
Published 30 March 2020

Abstract

A grid of 5285 *ab initio* points is utilized to construct a 3D potential energy surface (PES) of the $CH_2(\tilde{X}^3A'')$ system. In the calculation procedure, the aug-cc-pVXZ ($X = Q$ and 5) basis sets with Davidson correction are employed. The reference wave function for the multi-reference configuration interaction calculations is composed of a full valence complete-active-space self-consistent field wave function. In order to get a more accurate PES, the complete basis set (CBS) limit proposal and the many-body expansion form are used, with the total root mean square deviation of the final CBS-PES being 0.0349 eV. Based on the accurate $CH_2(\tilde{X}^3A'')$ CBS-PES, the stationary points and vibrational energy levels are obtained and examined in detail, which agree well with other theoretical results. Then, utilizing the CBS-PES and quasi-classical trajectory method, the integral cross-sections (ICSs) and rate constants of the $H(^2S) + CH(X^2\Pi) \rightarrow H_2(X^1\Sigma_g^+) + C(^3P)/CH(X^2\Pi) + H(^2S)$ reactions are calculated. It is found that the present ICSs are in good agreement with other theoretical results, and $H_2(X^1\Sigma_g^+) + C(^3P)$ is the major product channel. For this channel, the rate constants calculated in this work agree well with experimental and other theoretical results in the high-temperature range. It is worth noting that at room temperature, the theoretical results, including the present work, are consistent with each other, but they are all higher (about 7–10 times) than the experimental result, which implies that a new measurement for the rate constant at room temperature is necessary.

Supplementary material for this article is available online

Keywords: potential energy surface, quasi-classical trajectory method, rate constants

(Some figures may appear in colour only in the online journal)

1. Introduction

Because methylene molecule, CH_2, is not only a significant intermediate in numerous organic reactions, but plays a central role in astrochemical and combustion processes, it has attracted wide of interest of both astrophysicists and chemists for decades. To date, there have been a considerable number of theoretical works on potential energy surface (PES) for its different states [1–14]. Here, the attention is focused on the full-dimensional PES of CH_2, as well as its application in dynamics.

For the triplet electronic state of CH_2, its global PES was obtained in the least squares fitting procedure by employing 226 energy points calculated using the complete-active-space self-consistent field (CASSCF) method, and some spectroscopic data [3]. This PES can describe all asymptotic regions and has conical intersections along linear dissociations to CH + H. Based on the PES and quasi-classical trajectory

(QCT) method, Murrell and Dunne [15] studied the rate constants of the $CH(^2\Pi) + H(^2S) \rightarrow C(^3P) + H_2(^1\Sigma_g^+)$ reaction, and the calculated rate constant was 0.4×10^{-10} cm^3 molecule^{-1} s^{-1} at 2000 K. By fitting 45 and 24 *ab initio* energy points on the triplet and singlet surfaces, respectively, the PESs of the ground $\tilde{X}\ ^3B_1$ and first excited $\tilde{a}\ ^1A_1$ electronic states of CH_2, as well as rotation-vibration energy levels, were obtained [7].

The most accurate full-dimensional PES of $CH_2(\tilde{X}^3A'')$ was reported by Harding, Guadagnini and Schatz [9] (HGS PES). In this work, the multi-reference configuration interaction (MRCI) method, together with the polarized valence triple zeta, correlation consistent basis set of Dunning was used. The fitted HGS PES includes conical intersections between the $^3B_1$ and $^3A_2$ states for C_{2v} geometries and between the $^3\Pi$ and $^3\Sigma^-$ states for linear geometries. Then, the rate constants of the $CH(^2\Pi) + H(^2S) \rightarrow C(^3P) + H_2(^1\Sigma_g^+)$ reaction were obtained by using the QCT method, which agrees well with experimental studies at the high-temperature range (1500-2000 K) [16], but are nearly ten times larger than the measurement result at 297K [17]. The reaction probabilities, integral cross-sections (ICSs) and rate constants of the $CH(^2\Pi) + H(^2S) \rightarrow C(^3P) + H_2(^1\Sigma_g^+)$ reaction were obtained [18] by using a quantum-mechanical (QM) wavepacket and QCT methods based on HGS PES. It is shown that quantum effects are minor in the above reaction, and the QCT calculations can provide realistic estimates of ICSs and the rate constants. In 2012, Gamallo *et al* [19] investigated the $CH(^2\Pi) + H(^2S)$ reactions employing the QM method based on HGS PES. They analyzed the four lowest CH_2 electronic states in detail, performed a non-adiabatic test of Renner–Teller and spin–orbit on the $\tilde{X}^3A''$, $\tilde{a}\ ^1A'$ and $\tilde{b}\ ^1A''$ coupled PESs, and validated the $\tilde{X}^3A''$ Born–Oppenheimer (BO) results. The test confirms that these reactions occur essentially on the uncoupled $\tilde{X}^3A''$ ground surface. Subsequently, they further studied the BO and non-adiabatic Renner–Teller effects on $D(^2S) + CH(^2\Pi)$ reactions for three possible product channels: $C(^3P) + HD(^1\Sigma_g^+)$, $C(^1D) + HD(^1\Sigma_g^+)$ and $CD(^2\Pi) + H(^2S)$ using time-dependent real wavepacket and flux methods on $\tilde{X}^3A''$, $\tilde{a}\ ^1A'$ and $\tilde{b}\ ^1A''$ coupled PESs [20]. They found that the calculated rate constant of the $CH(^2\Pi) + H(^2S) \rightarrow C(^3P) + H_2(^1\Sigma_g^+)$ reaction agrees well with the QCT results [9, 21] at 297 K. However, the rate constant is still larger than that of experiment [17], so they suggested that the rate constant at room temperature should be re-measured. It should be noted that these two calculated theoretical results [9, 19] at room temperature are based on the same PES, which may lead to the same difference with the experimental one [17]. To test the validity of the calculations, in the present work, we construct a new PES using the set of 5285 *ab initio* points, and calculate the rate constant at room temperature again.

To study the $C(^1D) + H_2(^1\Sigma_g^+)$ reactions on the 3D PES, the singlet states of methylene molecule also cause widespread concern among researchers. The adiabatic global PESs of the CH_2 system for the first ($\tilde{a}\ ^1A'$) [12] and second ($1\ ^1A''$) [13] singlet states were obtained by Bussery-Honvault *et al*. Based on the adiabatic global PESs, accurate 3D QM scattering calculations were performed for the $C(^1D) + H_2(^1\Sigma_g^+) \rightarrow CH(^2\Pi) + H(^2S)$ reaction. The Coriolis coupling effects [22] and stereodynamic properties [23] of $CH(^2\Pi; v = 0, j = 1) + H(^2S) \rightarrow C(^1D) + H_2(^1\Sigma_g^+)$ and its isotopic variants H + CD, D + CH and D + CD were investigated by Lu *et al* using the $CH_2(\tilde{a}\ ^1A')$ PES. Soon after, a new accurate double many-body expansion (DMBE) PES of $CH_2(^1A')$ was reported by Joseph and Varandas [2] through fitting about 2500 corrected *ab initio* energy points. The DMBE PES shows good behavior over the entire configuration space, and its stationary point properties were carefully examined and compared with results calculated by other PESs, as well as experimental data, showing high accuracy. In 2014, Zhang *et al* [24] reported a global Zhang–Ma–Bian-a (ZMB-a) PES using 6300 *ab initio* energy points with MBE scheme. The ZMB-a PES covers the regions around conical intersections and of van der Waals interactions. Based on the above PES, many related dynamic investigations emerged [25–32], which are not given in detail here.

Through the above discussions, it is found that the singlet states of CH_2 are the focus topics, whereas there are relatively fewer investigations for the triplet ground state. And the previous theoretical rate constants at room temperature for the $H(^2S) + CH(X^2\Pi) \rightarrow H_2(X\ ^1\Sigma_g^+) + C(^3P)$ reaction differ greatly from the experimental data. The purpose of the present work is to verify whether the difference of rate constant between the previous theoretical and experimental results at room temperature is caused by the PES. Therefore, the primary objective is to get a high-quality 3D PES of $CH_2(\tilde{X}^3A'')$. To this end, the basis sets of aug-cc-pV*QZ* (AV*QZ*) and aug-cc-pV5Z (AV5Z) with Davidson correction are employed, and the calculated energy points are extrapolated to the complete basis set (CBS) limit, then the MBE scheme is employed to fit these corrected *ab initio* energy points. The detailed descriptions of CBS and MBE schemes are given

Table 1. Root mean square deviations of $CH_2(\tilde{X}^3A'')$ CBS-PES.

Energy[a]	N[b]	rmsd[a]	Max error[a]	$N >$ rmsd[c]
0.5	29	0.0071	0.0209	7
1.0	95	0.0095	0.0274	25
1.5	159	0.0096	0.0317	40
2.0	214	0.0113	0.0585	48
2.5	265	0.0164	0.0912	52
3.0	315	0.0241	0.1181	51
4.0	1542	0.0257	0.1384	284
5.0	2761	0.0326	0.2014	538
6.0	3597	0.0335	0.2014	718
7.0	4392	0.0337	0.2014	895
8.0	4959	0.0331	0.2014	1005
9.0	5019	0.0335	0.2014	1021
10.0	5106	0.0335	0.2014	1045
12.5	5178	0.0338	0.2014	1076
15.0	5232	0.0343	0.2014	1098
17.0	5285	0.0349	0.2014	1116

[a] The units of energy and rmsd are in eV.
[b] Number of points in the indicated energy range.
[c] Number of points with an energy deviation large than the rmsd.

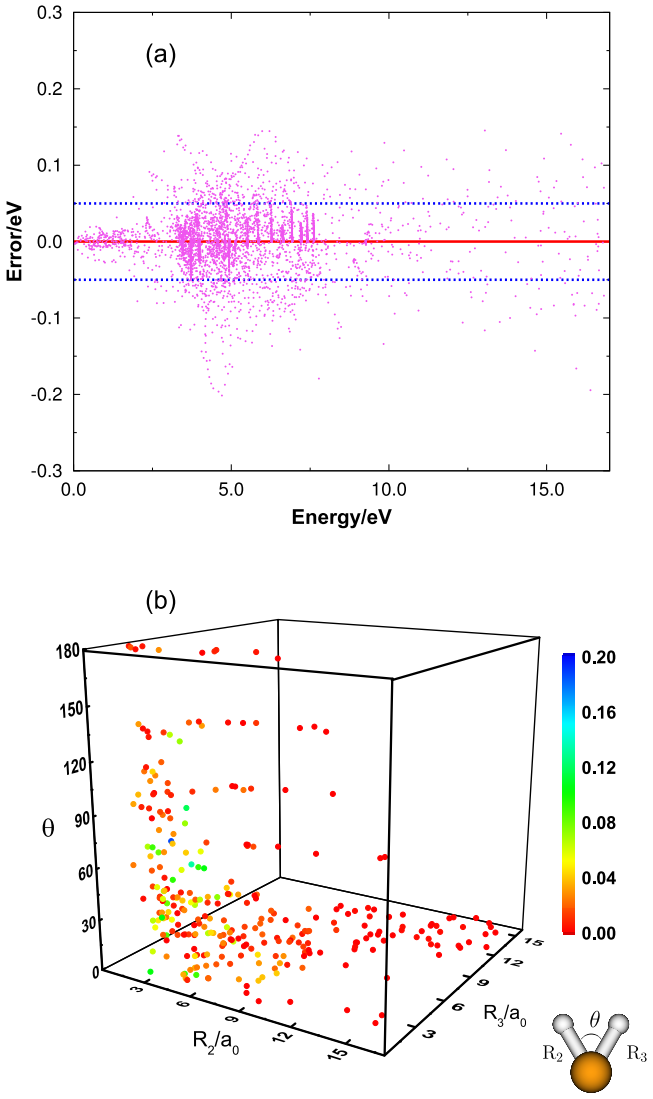

Figure 1. Fitting error distribution of the global PES of $CH_2(\tilde{X}^3A'')$ (a) in the energy domain; (b) in the coordinate space.

in section 2. Section 3 displays the main topographical features of this novel PES. The QCT and QM calculations of the $H(^2S) + CH(X^2\Pi) \rightarrow H_2(X\ ^1\Sigma_g^+) + C(^3P)/CH(X^2\Pi) + H(^2S)$ reactions based on the new PES are reported in section 4. The concluding remarks appear in section 5.

2. Methods

2.1. Ab initio calculations and extrapolation scheme

A total of 5285 *ab initio* points are calculated by the Molpro 2012 package [33] with AV*Q*Z and AV5Z basis sets [34, 35]. The *ab initio* calculations are carried out at MRCI level with Davidson corrections [MRCI(Q)] [36, 37] using the full valence CASSCF [38] wave function as reference. In the calculation, the C_s point group symmetry is employed, which holds two irreducible representations, namely, A′ and A″. For the $CH_2(\tilde{X}^3A'')$, five A′ and one A″ symmetry molecular orbitals are determined as the active space, amounting to 287 (177 A′ + 110 A″) configuration state functions. All energy points are over the $C - H_2$ channel defined by $1.4 \leqslant R_{H_2}/a_0 \leqslant 4.0$, $0.6 \leqslant r_{C-H_2}/a_0 \leqslant 15.0$ and $0 \leqslant \gamma/\mathrm{deg} \leqslant 90$, and the H-CH channel defined by $1.2 \leqslant R_{CH}/a_0 \leqslant 3.8$, $0.6 \leqslant r_{H-CH}/a_0 \leqslant 15.0$ and $0 \leqslant \gamma/\mathrm{deg} \leqslant 180$, where R, r and γ are the atom-diatom Jacobi coordinates for both channels.

The CBS limit scheme is one of the best tools to provide excellent PESs, which has been used to construct many other PESs [39–45]. In this scheme, each MRCI(Q) energy can be divided into two parts, CAS and dynamic correlation (dc) energies, which can be written as,

$$E(\mathbf{R}) = E_{\mathrm{CAS}}(\mathbf{R}) + E_{\mathrm{dc}}(\mathbf{R}). \tag{1}$$

In order to get the total CBS limit energies ($E^{\infty}(\mathbf{R})$), the $E_{\mathrm{CAS}}(\mathbf{R})$ and $E_{\mathrm{dc}}(\mathbf{R})$ must be extrapolated to the CBS limit, respectively. First, the $E_{\mathrm{CAS}}(\mathbf{R})$ is extrapolated to the limit ($E_{\mathrm{CAS}}^{\infty}(\mathbf{R})$) according to the formula expressed as [46],

$$E_{\mathrm{CAS}}^{X}(\mathbf{R}) = E_{\mathrm{CAS}}^{\infty}(\mathbf{R}) + B/X^{\alpha}, \tag{2}$$

where X represents the AVXZ ($X = Q$, 5) basis sets. $\alpha = 5.34$ is an effective decay parameter. Second, the $E_{\mathrm{dc}}(\mathbf{R})$ is extrapolated to the limit ($E_{\mathrm{dc}}^{\infty}(\mathbf{R})$) by utilizing the USTE protocol [47], which can been written as,

$$E_{\mathrm{dc}}^{X}(\mathbf{R}) = E_{\mathrm{dc}}^{\infty}(\mathbf{R}) + \frac{A_3}{(X+\alpha)^3} + \frac{A_5}{(X+\alpha)^5}, \tag{3}$$

and A_5 is determined by the following auxiliary relation:

$$A_5 = A_5(0) + cA_3^{5/4}, \tag{4}$$

where $A_5(0)$, c and α are the general constants [47], while $E_{\mathrm{dc}}^{\infty}(\mathbf{R})$ and A_3 are the unknowns to be determined from a fit to the dc energies.

2.2. PES of $CH_2(\tilde{X}^3A'')$

The $CH_2(\tilde{X}^3A'')$ is dissociated according to the following schemes:

$$CH_2(\tilde{X}^3A'') \rightarrow \begin{cases} H_2(X\ ^1\Sigma_g^+) + C(^3P) \\ CH(X^2\Pi) + H(^2S) \\ C(^3P) + H(^2S) + H(^2S) \end{cases}. \tag{5}$$

In the present work, the MBE [48, 49] function is employed to construct the $CH_2(\tilde{X}^3A'')$ PES, which has been widely used for triatomic systems [50–53], and is expressed as,

$$V_{\mathrm{ABC}}(\mathbf{R}) = \sum_{\mathrm{A}} V_{\mathrm{A}}^{(1)} + \sum_{\mathrm{AB}} V_{\mathrm{AB}}^{(2)}(R_{\mathrm{AB}}) + V_{\mathrm{ABC}}^{(3)}(R_{\mathrm{AB}}, R_{\mathrm{AC}}, R_{\mathrm{BC}}), \tag{6}$$

where $V_{\mathrm{A}}^{(1)}$ (C (^3P), H(^2S) and H(^2S)) is the energy of three isolated atoms, which can be set to zero because of the three isolated atoms being in the ground state. $V_{\mathrm{AB}}^{(2)}$ (AB = CH_a, CH_b, HH) and $V_{\mathrm{ABC}}^{(3)}$ are the energies of two-body and three-body terms.

Table 2. Attributes of stationary points on the $CH_2(\tilde{X}^3A'')$ CBS-PES.

Method	R_1/a_0	R_2/a_0	R_3/a_0	E^a	E^b	ω_1/cm^{-1c}	ω_2/cm^{-1c}	ω_3/cm^{-1c}
				Global Min C_{2v} ($^3B_1$)				
New PES[d]	3.740	2.036	2.036	8.2151	0.0	3155.61	1150.84	3395.87
MRCI/AVQZ	3.742	2.036	2.036	8.1756	0.0	3148.01	1131.16	3373.92
MRCI/AV5Z	3.740	2.036	2.036	8.1943	0.0	3150.59	1131.59	3377.11
HGS PES[e]	3.747	2.040	2.040	—	0.0	3130	1105	3355
JB PES[f]	3.741	2.033	2.033	—	0.0	3105	1090	3340
Thero.[g]	3.735	2.032	2.032	8.1915	—	—	—	—
Thero.[h]	3.747	2.040	2.040	8.2418	—	—	—	—
				H–C–H TS $D_{\infty v}$ ($^3\Sigma^-$)				
New PES[d]	4.019	2.009	2.009	7.9702	0.24	3336.72	936.77i	3582.53
MRCI/AVQZ	4.018	2.009	2.009	7.6687	0.388	3248.16	1039.08i	3583.73
MRCI/AV5Z	4.016	2.008	2.008	7.6866	0.387	3250.87	1036.71i	3587.93
HGS PES[e]	4.038	2.019	2.019	—	0.26	3200	1015i	3530
JB PES[f]	4.023	2.011	2.011	—	0.24	3170	983i	3515
				Local Min C_{2v} ($^3A_2$)				
New PES[d]	1.595	2.504	2.504	4.9824	3.23	1053.37	2051.97	1133.46
HGS PES[e]	1.707	2.471	2.471	—	3.18	1010	2685	1555
				C–H–H SP $C_{\infty v}$ ($^3\Pi$)				
New PES[d]	2.601	4.803	2.201	3.4367	4.78	1762.46	787.28i	1593.25i
HGS PES[e]	2.488	4.721	2.233	—	4.67	1810	1045i	1395i

[a] Energies are relative to the $C(^3P) + 2H(^2S)$ dissociation limit (in eV).
[b] Energies are relative to the $CH_2(\tilde{X}^3A'')$ global minimum (in eV).
[c] Harmonic vibrational frequencies (in cm^{-1}) for the symmetric (ω_1), bending (ω_2) and antisymmetric (ω_3) motions.
[d] This work. The PES is obtained at CBS-PES.
[e] [9].
[f] [6].
[g] [54] using MRCI/[13s12p10d8f6g4h2i/6s5p4d3f2g1h].
[h] [54] using RCCSD(T) method.

The two-body energy term, $V_{AB}^{(2)}$ (AB = CH_a, CH_b, HH), is obtained by the formalism [48, 49],

$$V_{AB}^{(2)} = \frac{\alpha_0}{R_{AB}} e^{-\beta_1^{(2)} R_{AB}} + \sum_{i=1}^{n} \alpha_i (R_{AB}\, e^{-\beta_2^{(2)} R_{AB}})^i, \qquad (7)$$

where the first term is called the short-range term, which guarantees that the energy approaches infinity as R_{AB}, the diatomic internuclear distance, is close to zero. And the latter is a long-range term, which warrants that the energy tends to zero when $R_{AB} \to \infty$. The constants of α_0, α_i ($i = 1, ...n$), β_1 and β_2 can be obtained by a nonlinear fitting process. In the current work, $n = 9$ and 11 for $CH(X^2\Pi)$ and $H_2(X\ ^1\Sigma_g^+)$ are found to be the optimal results. Since the potential curves of $CH(X^2\Pi)$ and $H_2(X\ ^1\Sigma_g^+)$ have been examined in detail in our previous works [43, 52], we employ them directly, and do not re-fit them here. However, for convenience to construct $CH_2(\tilde{X}^3A'')$ PES, the values of parameters employed to fit the $CH(X^2\Pi)$ and $H_2(X\ ^1\Sigma_g^+)$ potentials are still listed in table S1 of the Supporting Information (available online at stacks.iop.org/JPB/53/095202/mmedia) (SI).

The three-body term, $V_{ABC}^{(3)}$, is written as the Mth-order polynomial [48, 49]:

$$V_{ABC}^{(3)}(R_{AB}, R_{BC}, R_{AC}) = \begin{cases} \sum_{i,j,k=0}^{M} C_{ijk}\, \rho_{AB}^i \rho_{AC}^j \rho_{BC}^k & (j = k) \\ \sum_{i,j,k=0}^{M} C_{ijk}\, \rho_{AB}^i (\rho_{AC}^j \rho_{BC}^k + \rho_{BC}^j \rho_{AC}^k) & (j \neq k) \end{cases}, \qquad (8)$$

where $\rho_{AB} = R_{AB}\, e^{-\beta_{AB}^{(3)} R_{AB}}$, which is also applicable to the expressions of ρ_{AC} and ρ_{BC}. To ensure the three-body term goes to zero at all dissociation limits and at least one of the internuclear distances is zero, i, j and k should satisfy $i + j + k \neq i \neq j \neq k$ and $i + j + k \leqslant M$. In this work, M is set to be 10, which results in two nonlinear parameters (i.e. $\beta_{CH}^{(3)}$ and $\beta_{HH}^{(3)}$) and 140 linear coefficients C_{ijk} obtained in the fitting process, and the above parameters are all listed in table S2 of the SI. In order to ensure the permutation symmetry of two H atoms, two expressions as equation (8) are used.

The root mean squared deviation (rmsd) of the final $CH_2(\tilde{X}^3A'')$ CBS-PES is summarized in table 1, in which the energies are related to the CH_2 global minimum. From this table, it can be seen that by fitting 29 energy points, the rmsd is only 0.0071 eV and the maximum error is 0.0209 eV between 0.0–0.5 eV above global minimum. The new $CH_2(\tilde{X}^3A'')$ CBS-PES covers the energy range up to 17 eV above the global minimum by fitting a total of 5285 *ab initio* energy points, and the final rmsd is 0.0367 eV, showing high accuracy. To further verify the quality of the present CBS-PES, the fitting error distributions in the energy domain and in the coordinate space are shown in figure 1. As can be seen in panel (a), most of the error points are scattered between −0.05–0.05 eV (two blue dashed lines). Explicitly, there are 4578 points between two blue dashed lines, which is approximately 86.62% of the total points. 580 points are located in the ranges of 0.05–0.10 eV and −0.05–0.10 eV.

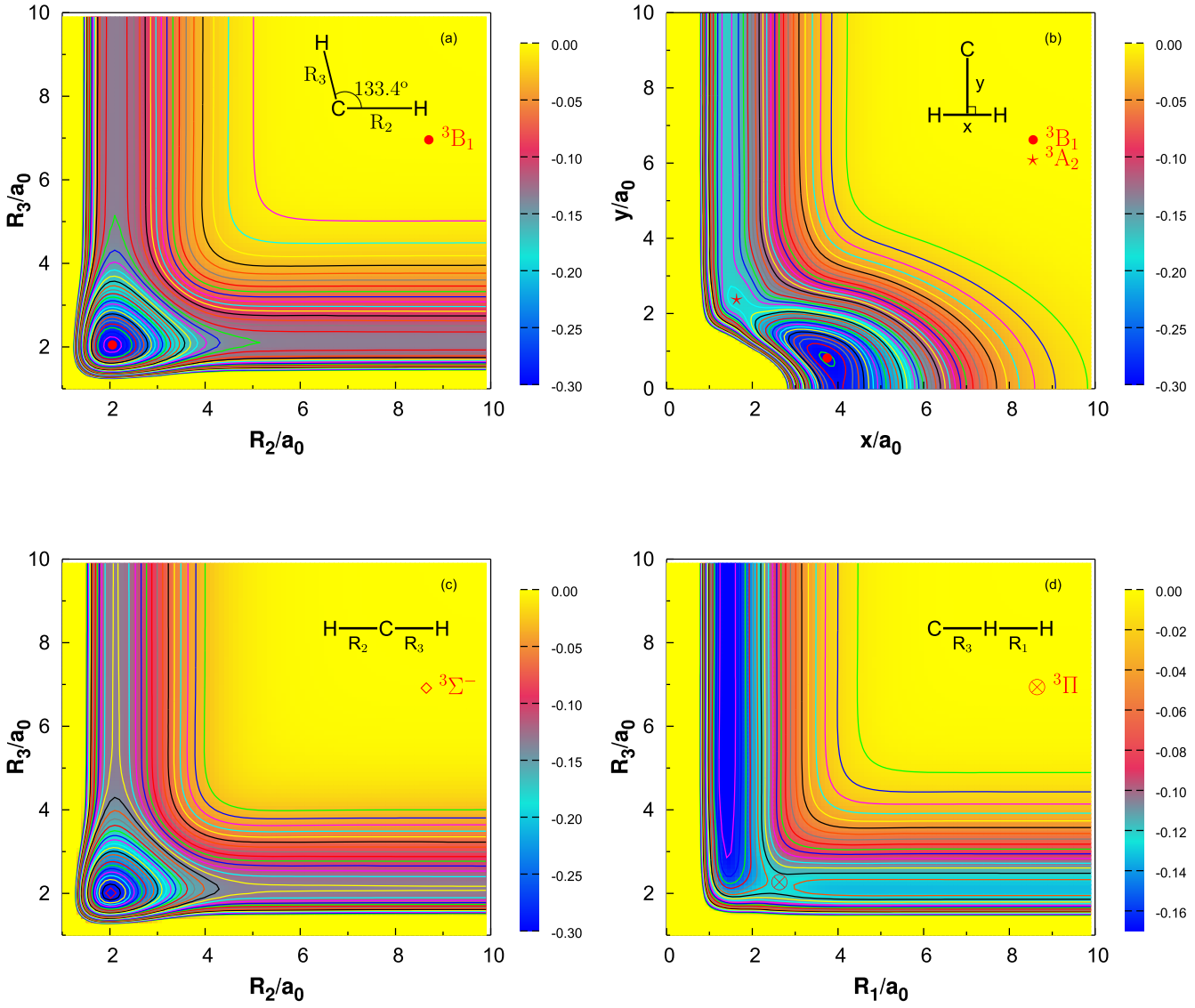

Figure 2. (a) Contour plot for bond stretching in H–C–H, keeping the included angle (∠[HCH]) fixed at 133.4°. (b) Contour plot for T-shaped insertion of C into H_2 diatom. (c) Contour plot for bond stretching in H–C–H linear configuration. (d) Contour plot for bond stretching in C–H–H linear configuration. Contours are equally spaced by 0.2177 eV, starting from −8.2451 eV for panel (a), −8.1634 eV for panel (b), −7.9757 eV for panel (c) and −4.800 eV for panel (d).

Moreover, there are only 127 points beyond 0.10 (−0.10) eV, occupying only 2.40% of the total points, which indicates that the present PES is of good quality. Panel (b) displays the fitting error distribution in the coordinate space, where R_2 and R_3 represent the C–H interatomic separations, θ is the angle between two C–H bonds and the error is the absolute value. It is easy to find that the energy points distribute throughout the whole space. Actually, the deviation is very small in the long range, especially as the length of R_2 or R_3 increases, the deviation tends to zero. It shows that the present PES is of high precision irrespective of whether it is in short range or long range, which is beneficial for the study of related dynamics (e.g. $CH(^2\Pi) + H(^2S) \rightarrow C(^3P) + H_2(^1\Sigma_g^+)$ /$CH(^2\Pi) + H(^2S)$).

3. Features of $CH_2(\tilde{X}^3A'')$

The properties of major stationary points on the $CH_2(\tilde{X}^3A'')$ CBS-PES are listed in table 2, including other theoretical results [6, 9, 54], as well as the results calculated with MRCI/AVQZ and MRCI/AV5Z methods. In order to observe the above major stationary points more intuitively, we marked them in figure 2, where R_1 represents the HH bond length, R_2 and R_3 the two CH ones, respectively. Panel (a) illustrates the contour map of $CH_2(\tilde{X}^3A'')$ CBS-PES for bond stretching in H–C–H structure, with the bending angle fixed at its equilibrium (∠HCH = 133.4°). The notable feature is the existence minimum ($^3B_1$) on the PES located at $R_1 = 3.740$ a_0,

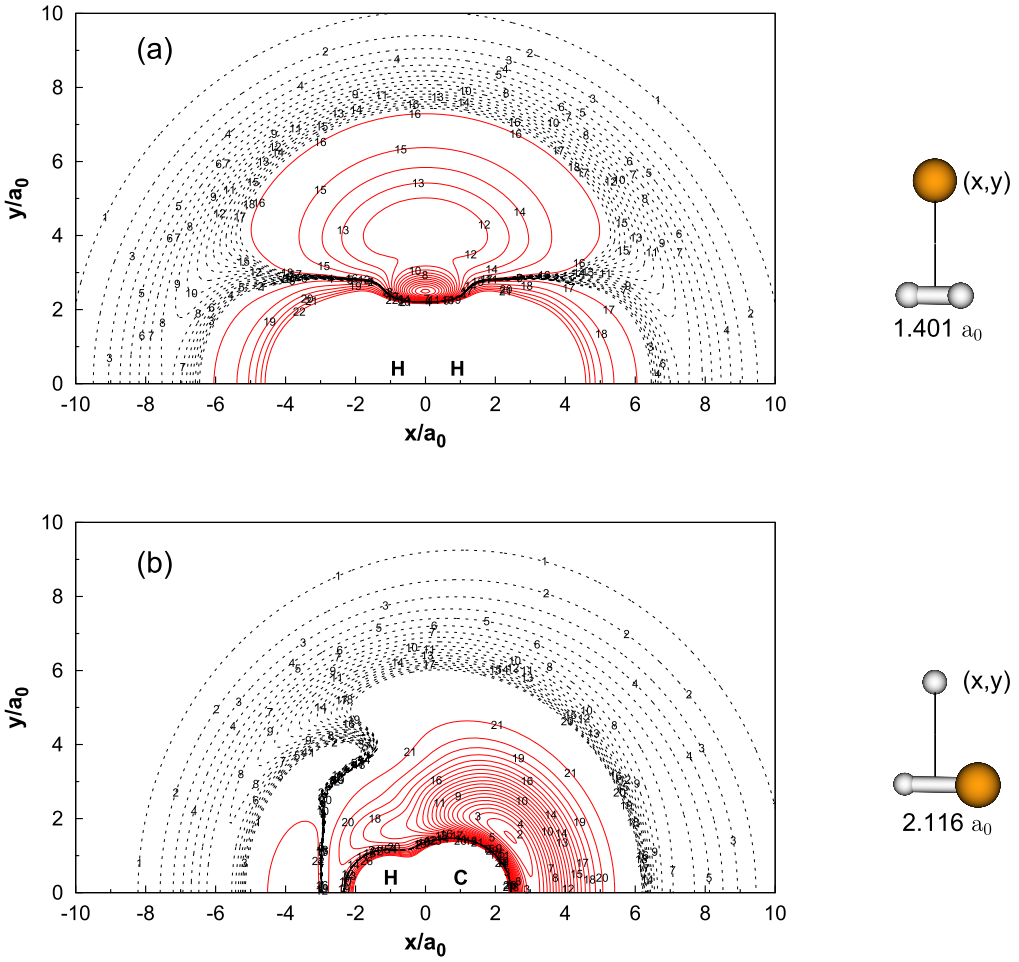

Figure 3. (a) Contour plot of potential energy when C moves around H_2 diatom fixed at its equilibrium geometry $R_{H_2} = 1.401\ a_0$ and lies along the *x*-axis with the center of the bond fixed at the origin. (b) Same as (a), but for H atom moving around CH fixed at the equilibrium geometry $R_{CH} = 2.116\ a_0$.

Table 3. Calculated vibrational energy levels (cm^{-1}) of $CH_2(\tilde{X}^3A'')$ for total angular momentum $J = 0$.

v_1	v_2	v_3	This work	Theor.[a]	Theor.[b]	Expt.
0	1	0	974.13	969	974	963.10[c]
0	2	0	1839.37	1837	1884	1829.97[d]
0	3	0	2815.72	2816	2821	2824.28[d]
1	0	0	3003.41	3013	3015	—
0	0	1	3219.22	3235	3236	—
1	1	0	3951.63	3973	3974	—
0	4	0	4053.37	4001	4007	4010.22[d]
0	1	1	4243.87	4220	4225	—

[a] [7] using MRCI method with Davidson correction.
[b] [7] using MRCI method.
[c] [55].
[d] [5] by fitting of the experimental energies using the nonrigid bender Hamiltonian.

$R_2 = 2.036\ a_0$ and $R_3 = 2.036\ a_0$, which is marked by a red solid point. This geometry agrees well with the results of HGS PES [9] and Jensen and Bunker (JB) PES [6], as shown in table 2, differing only by 0.007 a_0, 0.004 a_0, 0.004 a_0, and 0.001 a_0, 0.003 a_0, 0.003 a_0, respectively. And the results are also very close to the *ab initio* MRCI/AV*QZ* and MRCI/AV5Z results, especially for R_2 and R_3. Relative to the $C(^3P) + H(^2S) + H(^2S)$ dissociation limit, the well depth of the $^3B_1$ state is 8.2151 eV from the present work, which is found to be well consistent with the results of Kalemos *et al* [54]. The harmonic vibrational frequencies for the $^3B_1$ state calculated from the present CBS-PES are $\omega_1 = 3155.61\ cm^{-1}$, $\omega_2 = 1150.84\ cm^{-1}$ and $\omega_3 = 3395.87\ cm^{-1}$, while the differences are only 0.24%, 1.71% and 0.65% for MRCI/AV*QZ* results, 0.16%, 1.67% and 0.55% for MRCI/AV5Z results, and 0.81%, 3.98% and 1.20% for the results obtained with HGS PES [9].

The $^3B_1$ state can also be seen in figure 2 (b), which shows a contour plot for C atom attacking HH perpendicularly. In a Cartesian coordinate, the $^3B_1$ state is located at $x = 3.760\ a_0$, $y = 0.805\ a_0$, while the $^3A_2$ state is located at $x = 1.595\ a_0$, $y = 2.370\ a_0$. As illustrated in table 2, the $^3A_2$ state can be predicted by the present PES to be located at $R_1 = 1.595\ a_0$, $R_2 = 2.504\ a_0$ and $R_3 = 2.504\ a_0$, with the vibrational frequencies being $\omega_1 = 1053.37\ cm^{-1}$, $\omega_2 = 2051.97\ cm^{-1}$ and $\omega_3 = 1133.46\ cm^{-1}$. The calculated energy related to the $^3B_1$ state is 3.23 eV, which is slightly larger than that of the HGS PES result [9] of only 0.05 eV.

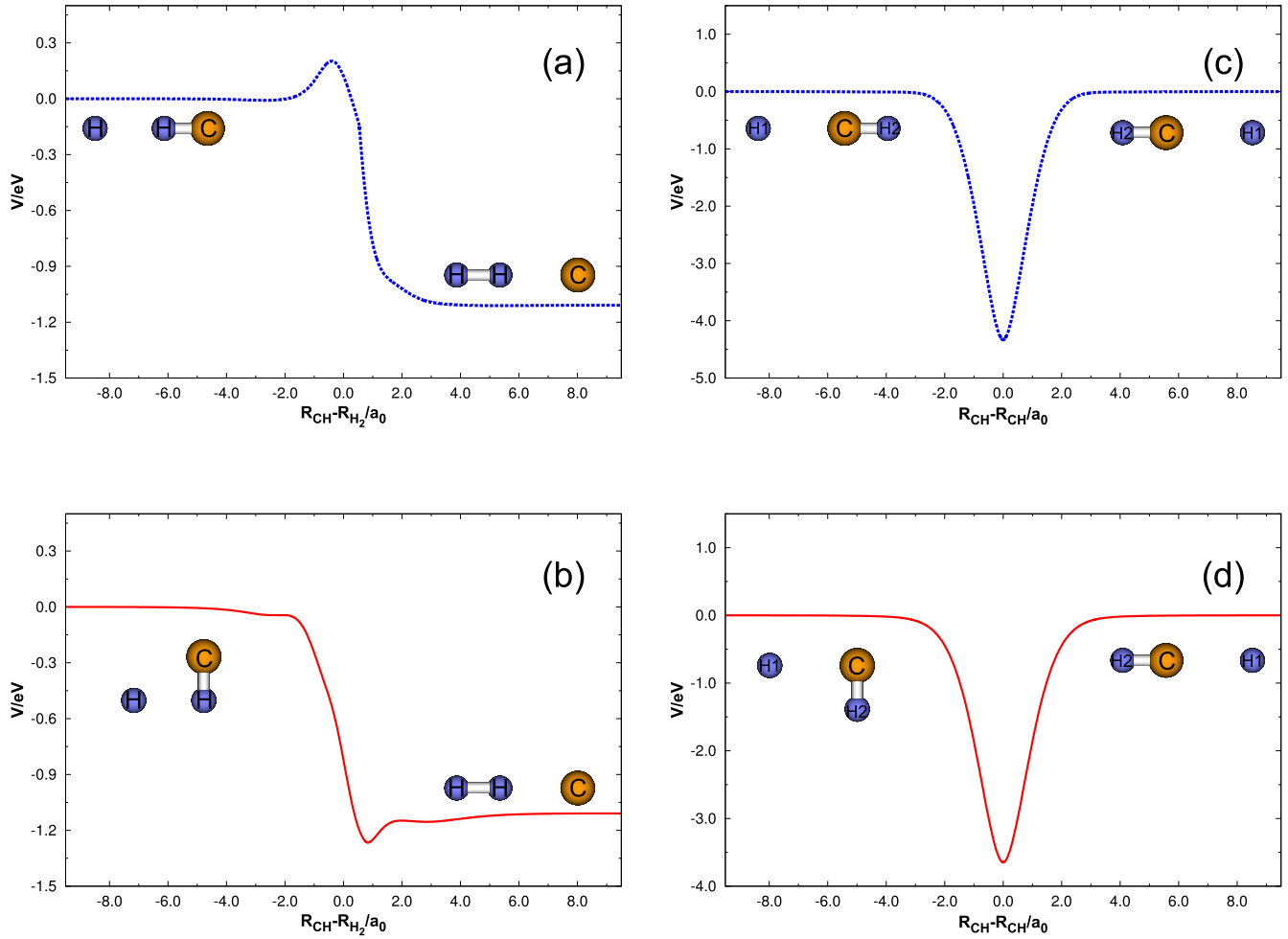

Figure 4. (a) and (b) Minimum energy path for the $H(^2S) + CH(X^2\Pi) \rightarrow H_2(X\ ^1\Sigma_g^+) + C(^3P)$ reaction as a function of $R_{CH} - R_{H_2}$ in collinear configuration and perpendicular configuration. (c) and (d) Same as (a) and (b), but for the $H(^2S) + CH(X^2\Pi) \rightarrow H(^2S) + CH(X^2\Pi)$ reaction as a function of $R_{CH} - R_{CH}$.

Table 4. Numerical parameters used in the Chebyshev wave packet calculation (atomic units unless otherwise stated).

	$R \in (10^{-16}, 16)$, $(N_R = 287)$
Grid/basis ranges and sizes	$r \in (0.5, 12)$, $(N_r = 207)$
	$\gamma \in (0, 180^o)$, $(N_\gamma = 50)$
Absorption potential	$R_d = 11.0$, $d_R = 0.0006$
	$r_d = 7.5$, $d_r = 0.001$
Initial wave packet	$R_0 = 0.8$; $E_0 = 0.15$ eV; $\delta = 0.15$
Spectral control	0.5
Position of the flux calculated	$r_f = 7.4$
Propagation steps	50000

Panels (c) and (d) of figure 2 display the contour plots for bond stretching in collinear H–C–H and C–H–H configurations. The notable feature in the former panel is the transition state (TS, denoted as $^3\Sigma^-$ state) at the $R_1 = 4.019\ a_0$, $R_2 = 2.009\ a_0$ and $R_3 = 2.009\ a_0$, lying at 0.24 eV above the global minimum energy. The differences of bond length are only 0.004 a_0, 0.002 a_0 and 0.002 a_0 with the results of JB PES [6], and the energies are the same in two decimal places. The present vibrational frequencies are $\omega_1 = 3336.72\ cm^{-1}$, $\omega_2 = 936.77i\ cm^{-1}$ and $\omega_3 = 3582.53\ cm^{-1}$, which agree well with the MRCI/AVQZ and MRCI/AV5Z results. Compared with the HGS PES results [9], they also agree well with each other, with the maximal difference of 7.71% occurring in ω_2. The notable feature in panel (d) is the saddle point (SP, denoted as $^3\Pi$ state) at $R_1 = 2.601\ a_0$, $R_2 = 4.803\ a_0$ and $R_3 = 2.201\ a_0$. These are in good agreement with the $R_1 = 2.488\ a_0$, $R_2 = 4.721\ a_0$ and $R_3 = 2.233\ a_0$ values reported by HGS PES [9]. According to the energy distribution shown in this plot, it is easy to find that the energy of the $^3\Pi$ state is higher than that of H + CH and C + HH channels, with the energies being 0.202 and 1.311 eV, respectively.

Figure 3 illustrates the energy contour for an atom going around the diatom fixed at its optimized geometry. The upper panel shows C atom going around the H_2 diatom fixed at its equilibrium distance $R_{H_2} = 1.401\ a_0$. The red solid lines are equally spaced by 0.0082 eV, starting at −4.8926 eV, while the black dotted lines are equally spaced by −0.0003 eV, starting at −4.7484eV. From this panel, it can be found that the $^3A_2$ state exists located at $x \sim 0.0000\ a_0$, $y \sim 2.4900\ a_0$. The contour plot for the H atom going around a fixed CH

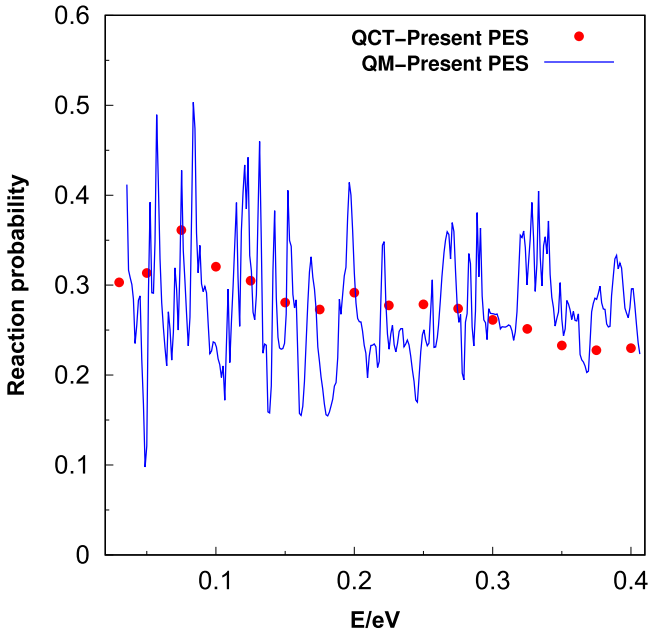

Figure 5. Comparison of the QM-computed reaction probability using the Chebyshev quantum wave packet method with the present QCT results for the H + CH reaction.

diatom whose bond length is fixed at the equilibrium geometry $R_{CH} = 2.116\ a_0$ is demonstrated in figure 3 (b). The contour starts at −8.1661 eV with equal spacing of 0.2176 eV for the red solid line. The black dotted lines are equally spaced by −0.0011 eV, starting at −3.6400 eV. As can be seen, there is a $^3B_1$ state at $x \sim 2.4499\ a_0$, $y \sim 1.4990\ a_0$, a $^3\Sigma^-$ state at $x \sim 3.0499\ a_0$, $y \sim 0.0000\ a_0$ and a $^3\Pi$ state at $x \sim -3.6001\ a_0$, $y \sim 0.0000\ a_0$. On the whole, these two plots display smooth behavior both at short and long range, which guarantees the high quality of the fitting procedure for the present PES.

Based on the present CBS-PES, the low-lying energy levels were calculated by the Lanczos algorithm, which can further verify the quality of the PES. The calculated vibrational energy levels, together with other theoretical [7] and experimental [5, 55] results, are tabulated in table 3. For convenient comparison, this table does not list the energy levels beyond 4500 cm^{-1}. The anharmonic vibrational frequencies (v_i, $i = 1, 2, 3$) are symmetric stretching, bending and antisymmetric stretching modes, respectively. It can be seen that the present energy levels are consistent with the other theoretical [7] and experimental [5, 55] data. For instance, the first vibrational energy level (0, 1, 0) in this work is calculated to be 974.13 cm^{-1}, which are only 5.13, 0.13 and 11.03 cm^{-1} larger than the other theoretical [7] and experimental [55] values. For the other vibrational energy levels, the current results are also found to be in good agreement with other theoretical [7] results using the MRCI method with Davidson correction, with the deviations being 0.13%, 0.01%, 0.32%, 0.49%, 0.54%, 1.29% and 0.56%, respectively. While the differences of (0, 2, 0), (0, 3, 0) and (0, 4, 0) energy levels between the current and experimental results [5] are respectively 0.51%, 0.30% and 0.97%, showing high accuracy.

4. Dynamical calculations

Figure 4 displays the minimum energy path (MEP) based on the $CH_2(\tilde{X}^3A'')$ CBS-PES. Panels (a) and (b) of this figure show the MEP of the $H(^2S) + CH(X^2\Pi) \rightarrow H_2(X\ ^1\Sigma_g^+) + C(^3P)$ reaction for the linear case ($\angle HHC = 180^o$) and vertical case ($\angle HHC = 90^o$), respectively. As displayed in both panels, R_{H_2} approaches the H_2 diatomic equilibrium bond length when the reaction coordinate is close to the larger positive values, while the larger negative reaction coordinate values are equivalent to R_{CH} approaching the CH diatomic equilibrium bond length. It can be easily found in panel (a) that a barrier of about 0.202 eV exists relative to H + CH reactant, which corresponds to the $^3\Pi$ state in the C–H–H configuration. And, there is a well about 1.265 and 0.156 eV relative to H + CH reactant and C + HH product, respectively, which corresponds to the $^3A_2$ state. Moreover, this reaction along the MEP is exoergic by 0.109 eV. Panels (c) and (d) respectively display the MEP of the $H(^2S) + CH(X^2\Pi) \rightarrow CH(X^2\Pi) + H(^2S)$ reaction for the linear case ($\angle HHC = 180^o$) and vertical case ($\angle HHC = 90^o$). Deep wells exist in these two panels, and the well of the upper panel corresponds to the $^3\Sigma^-$ state in the H–C–H construction.

Then, based on the present CBS-PES, the total reaction probabilities, ICSs and rate constants of the $H(^2S) + CH(X^2\Pi) \rightarrow H_2(X\ ^1\Sigma_g^+) + C(^3P)$ (denoted as R1) and $H(^2S) + CH(X^2\Pi) \rightarrow CH(X^2\Pi) + H(^2S)$ (denoted as R2) reactions are obtained by utilizing the QCT [56–59] and QM [60, 61] method. In QCT calculations, the initial distance (ρ_0) from the H atom to the center of mass of CH is 20 Å for the 10^5 trajectories, and the time integration step in the trajectories is chosen to be 0.1 fs. For the QM calculations, the optimum computational parameters determined in Jacobi coordinates are listed in table 4.

In order to prove that the QCT calculations can provide realistic estimates of ICSs and rate constants, the H + CH reaction probabilities are calculated based on the Chebyshev quantum wave packet method [60, 61], shown in figure 5 together with QCT results. Because the QM calculation is time consuming, we only calculated the reaction probability in $J = 0$. Due to the deep well on the MEP, the resonance structure exists in both results. It can also be found in this figure that the QCT reaction probabilities are close to the QM ones within the entire collision energy range, proving the validity of the QCT calculations. According to the above discussions, we have reason to believe that the QCT method is appropriate for studying the ICSs and rate constants of H + CH reaction, and the calculated ICSs and rate constants are all obtained based on the QCT method.

Figure 6 displays ICSs as a function of the collision energy for R1 and R2 at $j_0 = 0, 1, 3, 5, 7, 9$. For R1, due to the barrierless PES, the ICS first decreases rapidly and then decreases slowly with the increase of collision energy, which is very similar to other exothermic reactions [62–65]. In addition to this, the ICSs of R1 are much larger than those of

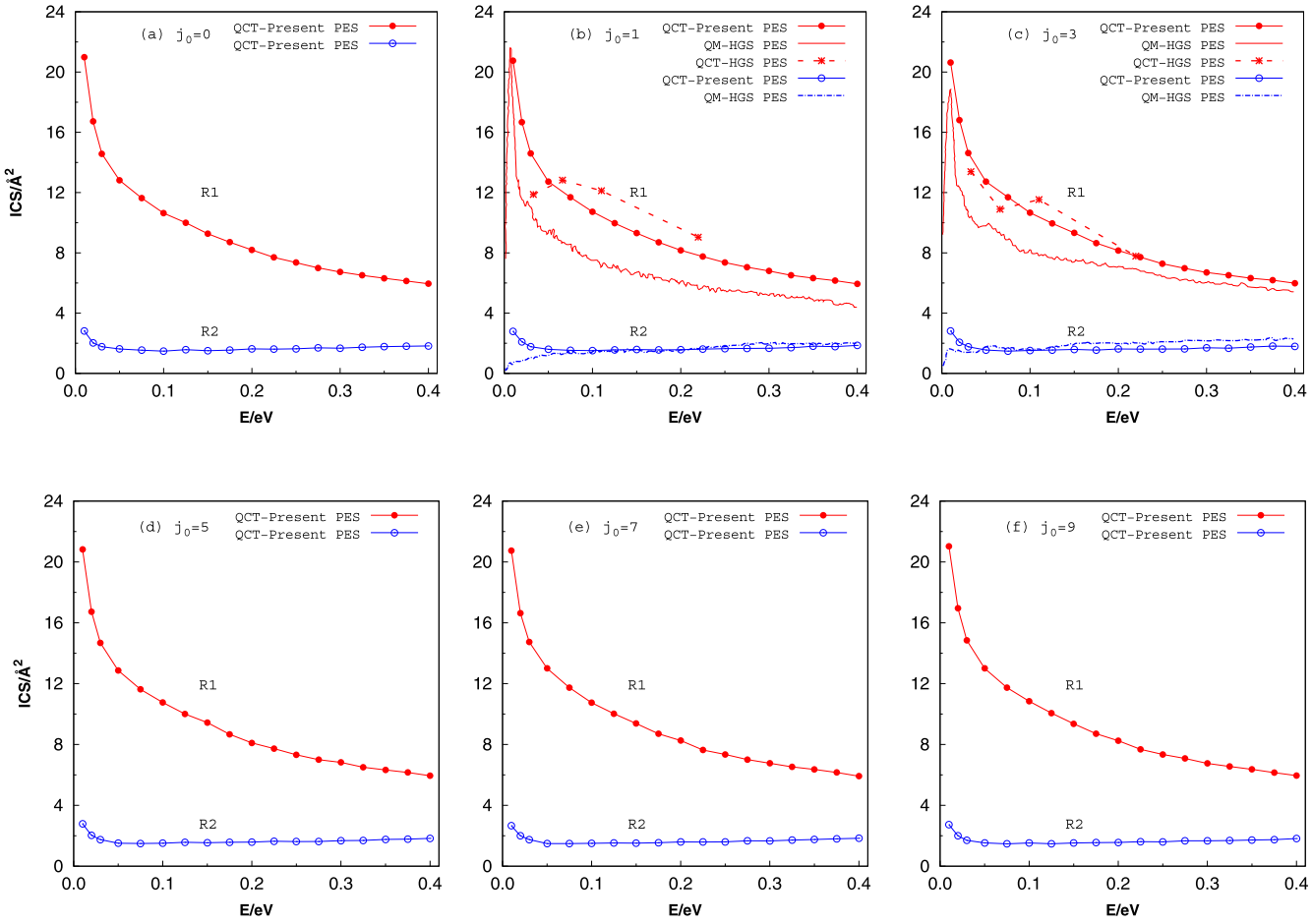

Figure 6. Integral cross-section as a function of the collision energy for R1 and R2 at $j_0 = 0$, 1, 3, 5, 7, 9.

Table 5. Rotationally-resolved rate constants $k/10^{-11}$ cm^3 s^{-1} for R1 and R2 at room temperature.

j_0	R1					R2	
	This work	Theor.[a]	Theor.[c]	Theor.[d]	Expt.[e]	This work	Theor.[a]
0	13.41	9.57 ± 0.96[b]	10.16	12.4	1.4 ± 0.5	1.72	1.41 ± 0.14[b]
1	13.39	10.8	—	—	—	1.73	1.13
3	13.40	11.0	—	—	—	1.70	1.71
5	13.45	9.76[b]	—	—	—	1.68	2.06[b]
7	13.50	—	—	—	—	1.66	—
9	13.59	—	—	—	—	1.66	—

[a] [19] using BO quantum-mechanical dynamics.
[b] [19] using cubic B-spline extrapolations.
[c] [9] using QCT method.
[d] [21] using QCT method by fitting $k = 12.4 \times 10^{-11}(T/300)^{0.26}$.
[e] [17].

R2, the curve of which is almost parallel to the x-axis. Furthermore, the ICSs depend slightly on the rotational quantum number j_0 of reactant CH, because the ICS values of R1 are between 20.63–21.02 Å^2 at 0.01 and 0.04 eV, and the values vary in the second decimal place (5.91 Å^2 −5.98 Å^2). At $j_0 = 1$ and 3, the ICSs obtained in the present CBS-PES are in excellent agreement with the results calculated by the QM [19] and QCT [9] based on HGS PES. The trend of present ICSs for R1 is consistent with that of QM within 0.01 and 0.40 eV, and the gap between the two results becomes smaller as the collision energy increases. For example, when $j_0 = 3$, the differences are about 4.46, 4.22, 2.94, 1.05, 1.04, 0.64, 0.60 and 0.56 Å^2 for 0.02, 0.03, 0.05, 0.20, 0.25, 0.30, 0.35 and 0.40 eV, respectively. For R2, when the collision energy is larger than 0.05 eV, the results obtained by the two methods are almost identical. However, when the collision energy is between 0.01–0.03 eV, there is an obvious gap between the two methods, which may be due to the well-known flaw in the

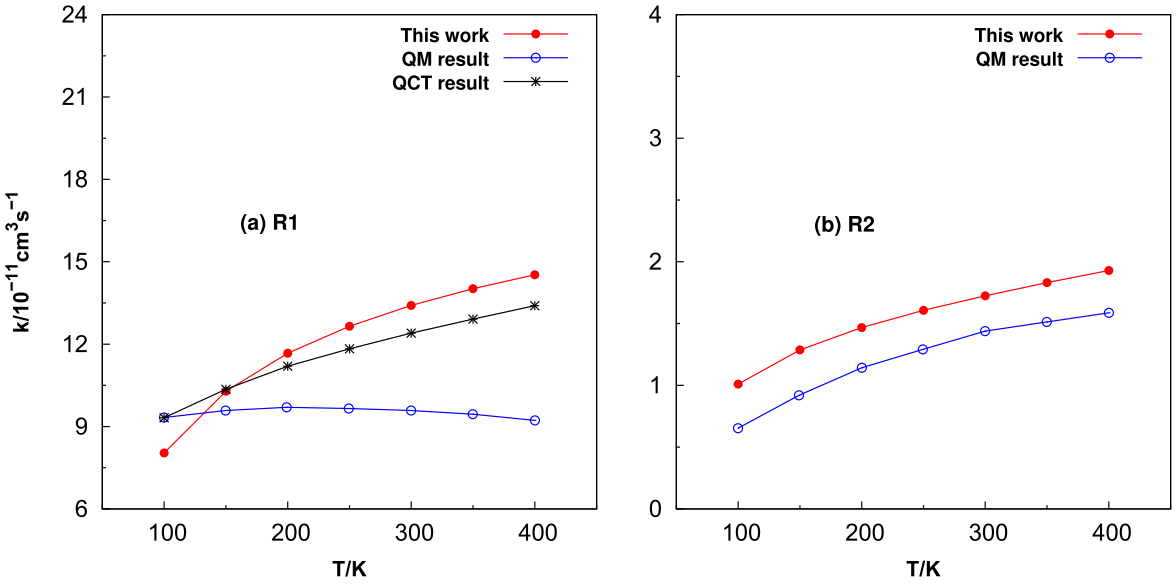

Figure 7. Rate constants for both reactions calculated in this work at lower temperatures, together with other theoretical results [19, 21].

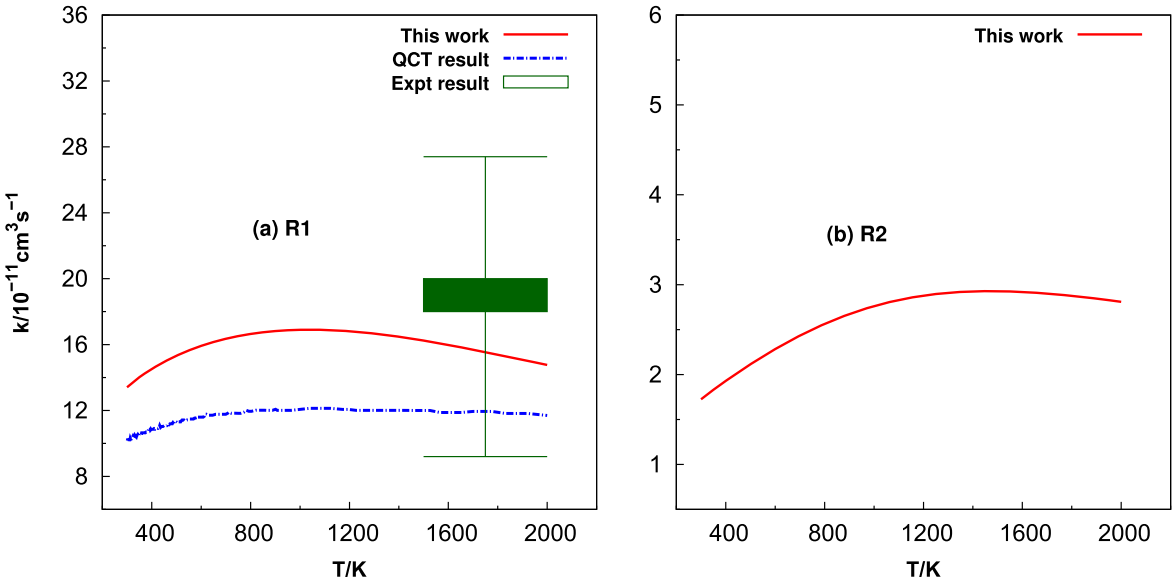

Figure 8. Rate constants for both reactions obtained in this work at higher temperatures, as well as other theoretical [9] and experimental [16] results.

QCT calculation [66, 67], in which zero-point energy is not considered.

Table 5 tabulates the rotational-resolved rate constants k at 300 K calculated in the present work, as well as other theoretical [9, 19, 21] and experimental [17] results. From this table, one can find that the rate constants vary a little as the rotational quantum number j_0 of reactant CH increases for two reactions, which is similar to the ICS results. For R1, comparing our results with QM [19], the differences are 3.84×10^{-11}, 2.59×10^{-11}, 2.4×10^{-11} and 3.69×10^{-11}cm^3 s^{-1} for $j_0 = 0$, 1, 3, 5, respectively. The rate constant of other QCT results [21] is 12.4×10^{-11}cm^3 s^{-1}, which agrees well with our result with a difference of only 1.01×10^{-11} cm^3 s^{-1}. Therefore, the computed rate constants are in good agreement with each other despite different theoretical methods and different PESs used. However, it can be easily found in this table that the experimental rate constant [17] at room temperature is lower than the theoretical results [9, 19, 21] including the present work, with the latter ones being about 7–10 times of the former one. With regard to the above discussion, we think that a new measurement of room temperature experimental rate constant is necessary. For the R2 reaction, comparing our results with QM [19], the differences are only 0.31×10^{-11}, 0.60×10^{-11}, 0.01×10^{-11} and 0.38×10^{-11}cm^3 s^{-1} for $j_0 = 0$, 1, 3, 5, respectively.

Figures 7 and 8 illustrate the rate constants at lower and higher temperatures, respectively. In the former figure, it can be found that the present values are higher than the values of the QM method [19] for two reactions, which may be due to the present ICS being larger than that of the QM method [19]. Note that the values and trends of rate constants obtained in

different methods and PESs are almost identical for R2. For R1, although the present rate constants slightly differ from the results of the QM method [19], there is good agreement with the QCT results [21], and the slight difference may be due to the different methods selected. In the latter one, it is easy to deduce that the discrepancy between two curves is small using the same method based on different PESs for R1 at higher temperatures. And the present results agree well with the experimental one [16] in the temperature range of 1500–2000 K, which is $(18.3 \pm 9.1) \times 10^{-11}$ cm^3 s^{-1}. Based on the above discussions, we have reason to believe that the results are reliable, although there are no other theoretical and experimental values to compare them with for R2 at high temperatures.

5. Conclusions

In the present work, we calculate plenty of *ab initio* energy points, and then employ the CBS limit proposal and MBE scheme to construct the 3D PES for $CH_2(\tilde{X}^3A'')$. The present CBS-PES covers energy up to 17 eV with rmsd being 0.0349eV. Such obtained CBS-PES can represent the properties (geometries, energies and vibrational frequencies) of the major stationary points and low-lying vibrational energy levels, which agree well with previous experimental and available theoretical results, and show the high quality of the CBS-PES. Based on the PES, the ICSs and rate constants of the $H(^2S) + CH(X^2\Pi) \rightarrow H_2(X\ ^1\Sigma_g^+) + C(^3P)$ (denoted as R1) and $H(^2S) + CH(X^2\Pi) \rightarrow CH(X^2\Pi) + H(^2S)$ (denoted as R2) reactions are obtained. As expected from MEPs for R1, the ICS first decreases rapidly and then decreases slowly with the increase of collision energies. And the ICSs depend slightly on the rotational quantum number j_0 of reactant CH for both reactions. In addition, by examining the ICSs, it is found that $H_2(X\ ^1\Sigma_g^+) + C(^3P)$ is the major product channel. It can also be found that the present ICSs are in good agreement with QM results, especially for R2. For rate constants, they agree well with other theoretical and experimental results in the high-temperature range for R1. However, at room temperature, despite the present work being consistent with other theoretical results, these results are all higher (about 7–10 times) than the experimental result. In order to further explore the reasons for this difference, it is suggested that other theoretical and experimental works be carried out.

Acknowledgments

This work was supported by the National Natural Science Foundation of China (Grant Nos. 11674198, 11874241 and 11904394), the Shandong Province Higher Educational Science and Technology Program (Grant No. J15LJ03), the Science Foundation of Shandong Jiaotong University (Grant Nos. Z201930 and Z201931) and the Ph.D. Research Start-up Fund of Shandong Jiaotong University (Grant No. 50004917).

ORCID iDs

Yuzhi Song https://orcid.org/0000-0002-2971-2824
Qingtian Meng https://orcid.org/0000-0003-2309-1307

References

[1] Blint R and Newton M 1975 *Chem. Phys. Lett.* **32** 178–83
[2] Joseph S and Varandas A J C 2009 *J. Phys. Chem. A* **113** 4175–83
[3] Knowles P J, Handy N C and Carter S 1983 *Mol. Phys.* **49** 681
[4] Harding L B 1983 *J. Chem. Phys.* **87** 441–6
[5] Bunker P R, Jensen P, Kraemer W P and Beardsworth R 1986 *J. Chem. Phys.* **85** 3724–31
[6] Jensen P and Bunker P R 1988 *J. Chem. Phys.* **89** 1327–32
[7] Comeau D C, Shavitt I, Jensen P and Bunker P R 1989 *J. Chem. Phys.* **90** 6491–500
[8] Beorda R A, van Hemert M C and van Dishoeck E F 1992 *J. Chem. Phys.* **97** 8240–9
[9] Harding L B, Guadagnini R and Schatz G C 1993 *J. Phys. Chem.* **97** 5472–81
[10] Yarkony D R 1996 *J. Phys. Chem.* **104** 2932–9
[11] Yarkony D R 1998 *J. Phys. Chem.* **109** 7047–50
[12] Bussery-Honvault B, Honvault P and Launay J M 2001 *J. Chem. Phys.* **115** 10701–8
[13] Bussery-Honvault B, Julien J, Honvault P and Launay J M 2005 *Phys. Chem. Chem. Phys.* **7** 1476–81
[14] Abdallah D B, Najar F, Jaidane N, Lakhdar Z B and Honvault P 2008 *Chem. Phys. Lett.* **456** 7–12
[15] Murrell J and Dunne L 1983 *Chem. Phys. Lett.* **102** 155–7
[16] Dean A J, Davidson D F and Hanson R K 1991 *J. Phys. Chem.* **95** 183–91
[17] Becker K H, Engelhardt B, Wiesen P and Bayes K D 1989 *Chem. Phys. Lett.* **154** 342–8
[18] van Harrevelt R, van Hemert M C and Schatz G C 2002 *J. Chem. Phys.* **116** 6002–11
[19] Gamallo P, Defazio P, Akpinar S and Petrongolo C 2012 *J. Phys. Chem. A* **116** 8291–6
[20] Gamallo P, Akpinar S, Defazio P and Petrongolo C 2015 *J. Phys. Chem. A* **119** 11254–64
[21] Loison J C and Honvault P 2011 Kinetic database for astrochemistry (http://kida.obs.u-bordeaux1.fr/)
[22] Lu R F, Wang Y H and Deng K M 2013 *J. Comput. Chem.* **34** 1735–42
[23] Wang Y H, Xiao C Y, Deng K M and Lu R F 2014 *Chin. Phys. B* **23** 43401
[24] Zhang C F, Fu M K, Shen Z T, Ma H T and Bian W S 2014 *J. Chem. Phys.* **140** 234301
[25] Joseph S, Caridade P J S B and Varandas A J C 2011 *J. Phys. Chem. A* **115** 7882–90
[26] Wu Y, Zhang C F, Cao J W and Bian W S 2014 *J. Phys. Chem. A* **118** 4235–42
[27] Shen Z T, Cao J W and Bian W S 2015 *J. Chem. Phys.* **142** 164309
[28] Hickson K M and Suleimanov Y V 2017 *Phys. Chem. Chem. Phys.* **19** 480–6
[29] Zhang C F, Zheng Y J, Cao J W and Bian W S 2017 *RSC Adv.* **7** 34348–55
[30] Sun Z P, Zhao W K and Yang C L 2017 *Int. J. Quantum. Chem.* **117** e25431
[31] González-Lezana T, Larrégaray P, Bonnet L, Wu Y N and Bian W S 2018 *J. Chem. Phys.* **148** 234305
[32] Wu Y N, Cao J W, Ma H T, Zhang C F, Bian W S, Nunez-Reyes D and Hickson K M 2019 *Sci. Adv.* **5** eaaw0446

[33] Knowles H-J *et al* 2012 Molpro (version 2012.1) a package of *ab initio* programs (http://www.molpro.net)
[34] Dunning T H Jr. 1989 *J. Chem. Phys.* **90** 1007–23
[35] Woon D and Dunning T H Jr. 1993 *J. Chem. Phys.* **98** 1358–71
[36] Werner H J and Knowles P J 1988 *J. Chem. Phys.* **89** 5803–14
[37] Knowles P J and Werner H J 1988 *Chem. Phys. Lett.* **145** 514–22
[38] Knowles P J and Werner H J 1985 *Chem. Phys. Lett.* **115** 259–67
[39] Song Y Z and Varandas A J C 2011 *J. Phys. Chem. A* **115** 5274–83
[40] Song Y Z and Varandas A J C 2009 *J. Chem. Phys.* **130** 134317
[41] Zhang L L, Gao S B, Meng Q T and Song Y Z 2015 *Chin. Phys. B* **24** 013101
[42] Zhang L L, Zhang J, Meng Q T and Song Y Z 2015 *Phys. Scr.* **90** 035403
[43] Zhang L L, Gao S B, Meng Q T, Pan J and Song Y Z 2018 *J. Chem. Phys.* **149** 154303
[44] Zhang L L, Song Y Z, Gao S B and Meng Q T 2018 *J. Phys. Chem. A* **122** 4390–8
[45] Gao F, Zhang L L, Zhao W L, Meng Q T and Song Y Z 2019 *J. Chem. Phys.* **150** 224304
[46] Karton A and Martin J M L 2006 *Theor. Chem. Acc.* **115** 330–3
[47] Varandas A J C 2007 *J. Chem. Phys.* **126** 244105244105–19
[48] Aguado A and Paniagua M 1992 *J. Chem. Phys.* **96** 1265–75
[49] Aguado A, tablero C and Paniagua M 1998 *Comp. Phys. Comm.* **108** 259–66
[50] Song Y Z, Zhang Y, Zhang L L, Gao S B and Meng Q T 2015 *Chin. Phys. B* **24** 063101
[51] Song Y Z, Zhang Y, Gao S B, Meng Q T, Wang C K and Ballester M Y 2018 *Mol. Phys.* **116** 129–41
[52] Song Y Z, Zhang L L, Gao S B and Meng Q T 2016 *Sci. Rep.* **6** 37734
[53] Guo L, Ma H Y, Zhang L L, Song Y Z and Li Y Q 2018 *RSC. Adv.* **8** 13635–42
[54] Kalemos A, Dunning T H Jr., Mavridis A and Harrison J F 2014 *Can. J. Chem.* **82** 684–93
[55] Marshall M D and McKellar A R W 1986 *J. Chem. Phys.* **85** 3716–23
[56] Wang M L, Han K L and He G Z 1998 *J. Chem. Phys.* **109** 5446–54
[57] Chen M D, Han K L and Lou N Q 2003 *J. Chem. Phys.* **118** 4463–70
[58] Chen M D, Han K L and Lou N Q 2002 *Chem. Phys. Lett.* **357** 483–90
[59] Wang M L, Han K L and He G Z 1998 *J. Phys. Chem. A* **102** 10204–10
[60] Lin S Y and GUO H 2003 *J. Chem. Phys.* **119** 11602
[61] Lin S Y and GUO H 2006 *J. Chem. Phys.* **124** 031101
[62] Gao S B, Zhang L L, Song Y Z and Meng Q T 2016 *Chem. Phys. Lett.* **651** 233–7
[63] Zhang L L, Gao S B, Song Y Z, Yue D G, Chen G M and Meng Q T 2017 *Can. J. Phys.* **95** 1219–24
[64] Zhang L L, Gao S B, Song Y Z and Meng Q T 2018 *J. Phys. B: At. Mol. Opt. Phys.* **51** 065202
[65] Song Y Z, Zhang L L, Cao E, Meng Q T and Ballester M Y 2017 *Theor. Chem. Acc.* **136** 38
[66] Varandas A J C 1994 *Chem. Phys. Lett.* **225** 18–27
[67] Schinke R and Fleurat-Lessard P 2005 *J. Chem. Phys.* **122** 094317